Two-Dimensional Boron Phosphide/MoGe$_2$N$_4$ van der Waals Heterostructure: A Promising Tunable Optoelectronic Material

Cuong Nguyen, Nguyen V. Hoang, Huynh V. Phuc, Ang Yee Sin, and Chuong V. Nguyen*

Read Online

ACCESS | Metrics & More | Article Recommendations

ABSTRACT: A van der Waals (VDW) heterostructure offers an effective strategy to create designer physical properties in vertically stacked two-dimensional (2D) materials, and offers a new paradigm in designing novel 2D heterostructure devices. In this work, we investigate the structural and electronic features of the BP/MoGe$_2$N$_4$ heterostructure. We show that the BP/MoGe$_2$N$_4$ heterostructure exists in a multiple structurally stable stacking configuration, thus revealing the experimental feasibility of fabricating such heterostructures. Electronically, the BP/MoGe$_2$N$_4$ heterostructure is a direct band gap semiconductor exhibiting type-II band alignment, which is highly beneficial for the spatial separation of electrons and holes. Upon forming the BP/MoGe$_2$N$_4$ heterostructure, the band gap of the constituent BP and MoGe$_2$N$_4$ monolayers are substantially reduced, thus allowing the easier creation of an electron−hole pair at a lower excitation energy. Interestingly, both the band gap and band alignment of the BP/MoGe$_2$N$_4$ heterostructure can be modulated by an external electric field and a vertical strain. The optical absorption of the BP/MoGe$_2$N$_4$ heterostructure is enhanced in both the visible-light and ultraviolet regions, thus suggesting a strong potential for solar cell application. Our findings reveal the promising potential of the BP/MoGe$_2$N$_4$ vdW heterostructure in high-performance optoelectronic device applications.
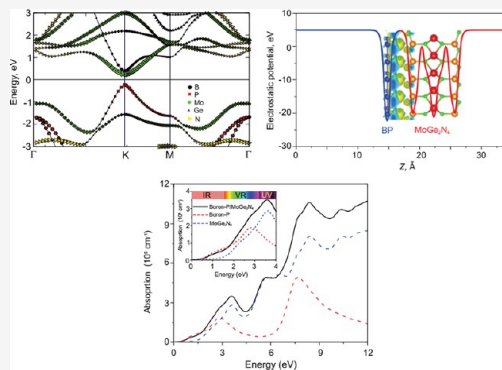
Two-dimensional (2D) materials, including graphene,[1] transition metal dichalcogenide, and black phosphorus[2−9] have enormous research interest due to their structural, electronic, optical, and transport properties, many of which are highly beneficial for a wide array of device applications. For example, graphene is known to have an ultrahigh carrier mobility[10] that makes it promising for nanoelectronic devices, such as an ultrafast photodetector.[11] The strong spin−orbit coupling in layered transition metal dichalcogenides[12,13] makes them suitable for spintronics applications. Beyond pristine monolayer and few-layer, different species of 2D materials can also be vertically stacked to form van der Waals (vdW) heterostructures. The vdW engineering of 2D materials offers a novel route to artificially create "designer" 2D hybrid materials with a wide array of physical properties to meet the varying demands of nanodevice applications.

The enormous design flexibility of the vdW heterostructure thus greatly expands the application capability of 2D materials. Recently, vdW heterostructures, composed of various combinations of graphene, phosphorene, MoS$_2$, WS$_2$, and so on, have been extensively studied, and many of these structures have been experimentally fabricated, such as graphene-based vdW heterostructures,[14−20] phosphorene-based heterostructures,[21−23] MoS$_2$-based heterostructures,[24−26] and so forth.

A new kind of 2D material, transition metal nitride (TMN) has received tremendous attention recently.[27,28] In 2020, the successful fabrication of MoSi$_2$N$_4$ (MSN) monolayers using a chemical vapor deposition (CVD) approach opened up a new avenue toward the expansive synthetic 2D material family of MA$_2$Z$_4$.[29] The atomic structure of monolayer MSN comprises a MoN$_2$ monolayer sandwiched by two Si−N bilayers. Recent first-principle calculations[28,30,31] have revealed the highly unusual physical properties of the MA$_2$N$_4$ family. Particularly, the TMN monolayer of this family, such as MoSi$_2$N$_4$ and MoGe$_2$N$_4$, are predicted to be promising candidates for optoelectronic and photocatalytic nanodevices owing to their Type-II band alignments and strong visible light absorption. The MA$_2$Z$_4$ family is thus expected to offer a new material platform to explore the unusual light−matter interactions of 2D-confined electrons.

On the other hand, a new type of graphene-like group III−V compounds, namely hexagonal boron phosphide (BP), has been predicted theoretically.[32,33] This material is known to be structurally stable at room temperature.[33] Monolayer BP has a
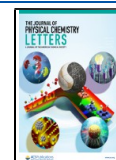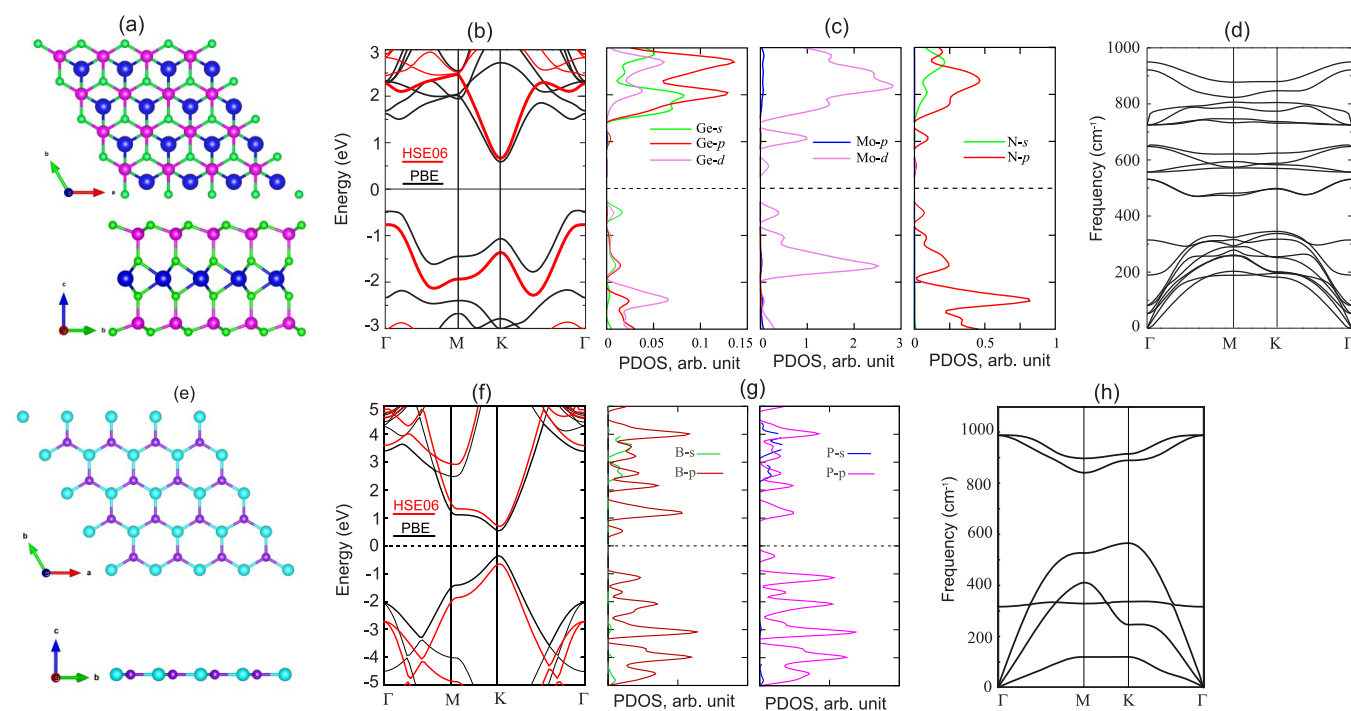
Figure 1. (a) Top and side views of the optimized atomic structure; (b) band structure calculated by PBE and HSE06 methods; (c) PDOS and (d) phonon spectrum of single-layer MoGe$_2$N$_4$ monolayer. (e) Top and side views of the optimized atomic structure, (f) calculated PBE and HSE06 band structures; (g) PDOS and (h) phonon spectrum of single-layer BP monolayer.

planar honeycomb structure with a direct band gap of about 0.82−1.81 eV, depending on the calculation methods.[32] Because of its graphene-like lattice and semiconducting nature, the physical properties and the device application potential of BP has been actively studied in recent years.[34−37]

In this work, we perform a pilot study to explore the synergy of BP and MoGe$_2$N$_4$ monolayers in vdW heterostructure engineering by first principle calculations. The structural, electronic, and optical properties of BP/MoGe$_2$N$_4$ vdW heterostructures under various stacking configurations are investigated. By calculating the phonon spectrum, we demonstrate the existence of a large array of structurally stable stacking configurations, thus concretely establishing the feasibility of BP/MoGe$_2$N$_4$ heterostructures. We show that BP/MoGe$_2$N$_4$ conveniently exhibits a Type-II band alignment, which is highly beneficial for electron−hole separation. The optical spectrum of BP/MoGe$_2$N$_4$ exhibits enhanced absorption in the visible to ultraviolet regimes. Intriguingly, the band alignment can be controlled via an external electric field or mechanical strain. Particularly, the Type-I-to-Type-II band alignment transition can be achieved with an electric field strength of 0.15 V/Å, which is close to the experimentally achievable value.[38] Our results reveal the potential of BP/MoGe$_2$N$_4$ heterostructure as a novel field- and strain-tunable optoelectronic material, thus opening up a new route toward the development of vdW heterostructure devices via the synergy of BP and MA$_2$Z$_4$ monolayer families.

All calculations in this work are performed through density functional theory (DFT), which is implemented in the simulated Quantum Espresso package.[39,40] The Perdew−Burke−Ernzerhof (PBE) functional in the framework of the generalized gradient approximation (GGA[41]) is used to describe the correlation-exchange energy, whereas the projected augmented wave (PAW) pseudopotential[42] is

adopted to describe the ion-electron bonding. The energy cutoff is calculated to be 500 eV for all calculations, which were fully optimized until the convergence of force and energy. The Brillouin zone (BZ) integration is sampled within a 9 × 9 × 1 k-point mesh. To avoid the bonding between the periodic sublayers, we set a large vacuum thickness of 25 Å. The Heyd−Scuseria−Ernzerhof hybrid functional (HSE06) is also used to obtain a more accurate value of band gaps. The weak vdW bondings in heterostructures are described by adding the vdW dispersion in the DFT-D3 approximation.[43]

We first investigate the structural and electronic properties of constituent BP and MGN monolayers in their single-layered form, as illustrated in Figure 1. The atomic structure of single-layer MoGe$_2$N$_4$ in Figure 1a demonstrates that it has a space group of $P6m1$ with a hexagonal crystal. The crystal of MoGe$_2$N$_4$ monolayer is composed of a MoN$_2$ monolayer sandwiched by two buckled Ge−N bilayers. The MoGe$_2$N$_4$ monolayers consist of seven layers, including 4 N layers, 2 Ge layers, and 1 Mo layer. The thickness of the MoGe$_2$N$_4$ monolayer is 10.60 Å. The optimized lattice constant of MGN is 3.04 Å, which is in good agreement with the previous reports.[28] The band structure of single-layer MoGe$_2$N$_4$ calculated by PBE and HSE06 is depicted in Figure 1b. Both the PBE and HSE06 predict the same semiconducting phase with an indirect band gap of 1.03 and 1.42 eV, respectively, which are in good agreement with the previous reports.[28,29] The conduction band minimum (CBM) of the MoGe$_2$N$_4$ monolayer is located at the K point, while the valence band maximum (VBM) lies along the K-Γ path for both the PBE and HSE06 methods. The projected density of states (PDOS) of all atoms in the MoGe$_2$N$_4$ monolayer is depicted in Figure 1c. We find that the CBM of such material is mainly attributable to the Mo-d orbital, while its VBM comes from the strong hybridization between Mo-d, N-p, and Ge-s orbitals.
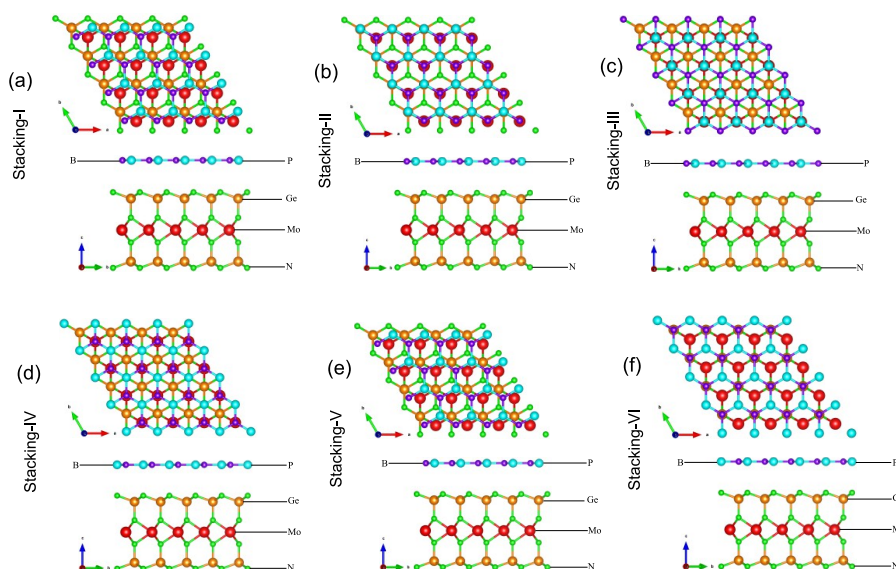
Figure 2. Top and side views of the optimized atomic structures for different stacking configurations of the BP/MoGe$_2$N$_4$ heterostructures. (a) stacking-I, (b) stacking-II, (c) stacking-III, (d) stacking-IV, (e) stacking-V, and (f) stacking-VI.

The phonon dispersion curves of the MoGe$_2$N$_4$ monolayer is also plotted in Figure 1d to check the stability. All the frequencies of the MoGe$_2$N$_4$ monolayer are positive at the ground state, confirming the structural stability of such material.

The structural and electronic features of pristine BP are illustrated in Figure 1e−h. BP monolayer has a planar hexagonal structure similar to that of graphene. The optimized lattice parameter of single-layer BP is calculated to be 3.20 Å. The band gap of pristine BP is 1.0 eV/1.42 eV obtained by the PBE/HSE06 method, as depicted in Figure 1f. These values of band gap are in good agreement with the previous data.[32,33] We can also see that both the PBE and HSE06 predict a direct band gap semiconducting characteristic, in which both the VBM and CBM locate at the K point. The PDOS of all atoms in the BP monolayer is depicted in Figure 1g. The VBM of the BP monolayer is mainly attributable to the strong hybridization between the B-$s(p)$ and P-$s(p)$ orbitals. The sp^2 hybridization thus exists in the valence band of the BP monolayer. The phonon spectrum of the BP monolayer is displayed in Figure 1h, which confirms the structural stability of material without any negative frequencies.

We construct the heterostructure by stacking BP on MoGe$_2$N$_4$ layers. We consider six different stacking configurations of BP/MoGe$_2$N$_4$ heterostructures. The lattice constant of the BP/MoGe$_2$N$_4$ heterostructure is 3.12 Å. This means that the lattice mismatch in the BP/MoGe$_2$N$_4$ heterostructure is calculated to be 2.56%, which provides little influence on the electronic properties and interfacial characteristics of the heterostructure. All stacking configurations are fully relaxed. The optimized atomic structures of all these configurations are depicted in Figure 2. The obtained interlayer distances of BP/MoGe$_2$N$_4$ heterostructure for all stacking configurations are listed in Table 1. The Stacking-II configuration of BP/MoGe$_2$N$_4$ heterostructure has the shortest interlayer distance of 3.08 Å when compared to others. The interlayer distance between BP and MoGe$_2$N$_4$ monolayers in their heterostructure is defined as the interlayer distance between the phosphorus layer of the BP monolayer and the topmost nitrogen layer of the MoGe$_2$N$_4$ monolayer. More

Table 1. Calculated Interlayer Spacing (d), Binding Energy (E_b), Band Gap Obtained by PBE and HSE06, and the Band Alignment and Work Function (W_F) of BP/MoGe$_2$N$_4$ Heterostructure for All Stacking Configurations

patterns	d, Å	E_b, meV/Å^2	E_g, eV PBE	E_g, eV HSE06	band alignment	W_F, eV
stacking-I	3.29	−54.92	0.36	0.65	type-II	5.40
stacking-II	3.08	−67.28	0.47	0.77	type-II	5.31
stacking-III	3.30	−55.62	0.39	0.68	type-II	5.32
stacking-IV	3.38	−36.56	0.41	0.72	type-II	5.35
stacking-V	3.26	−41.25	0.34	0.63	type-II	5.33
stacking-VI	3.32	−40.04	0.34	0.62	type-II	5.41

interestingly, we find that the interlayer distances of BP/MoGe$_2$N$_4$ heterostructure for different stacking configurations are in the range from 3.08 to 3.38 Å. These values of such interlayer distances are the same as those in other typical vdW heterostructures, such as graphite. In addition, these values of the interlayer distances of BP/MoGe$_2$N$_4$ heterostructure correlate well with the sum of the vdW radii for phosphorus (1.80 Å) and nitrogen (1.54 Å). All these findings demonstrate that the BP/MoGe$_2$N$_4$ heterostructure is thus a typical vdW heterostructure with the weak vdW interactions dominating the interaction between the BP and MoGe$_2$N$_4$ layers.

To check the structural stability of these configurations, we calculate their binding energies as follows:

$$E_b = \frac{E_H - E_{BP} - E_{MGN}}{S} \tag{1}$$

Here, E_H, E_{BP}, and E_{MGN}, respectively, are the total energies of the composed BP/MoGe$_2$N$_4$ heterostructure, isolated BP, and MoGe$_2$N$_4$ monolayers. S is the surface area of the considered heterostructure. The calculated binding energies BP/MoGe$_2$N$_4$ heterostructure for all stacking configurations are listed in Table 1. The stacking-II exhibits the lowest binding energy compared to that in other stacking configurations. The stacking-II is the most energetically favorable stacking configuration. Therefore, we focus on BP/MoGe$_2$N$_4$ hetero-
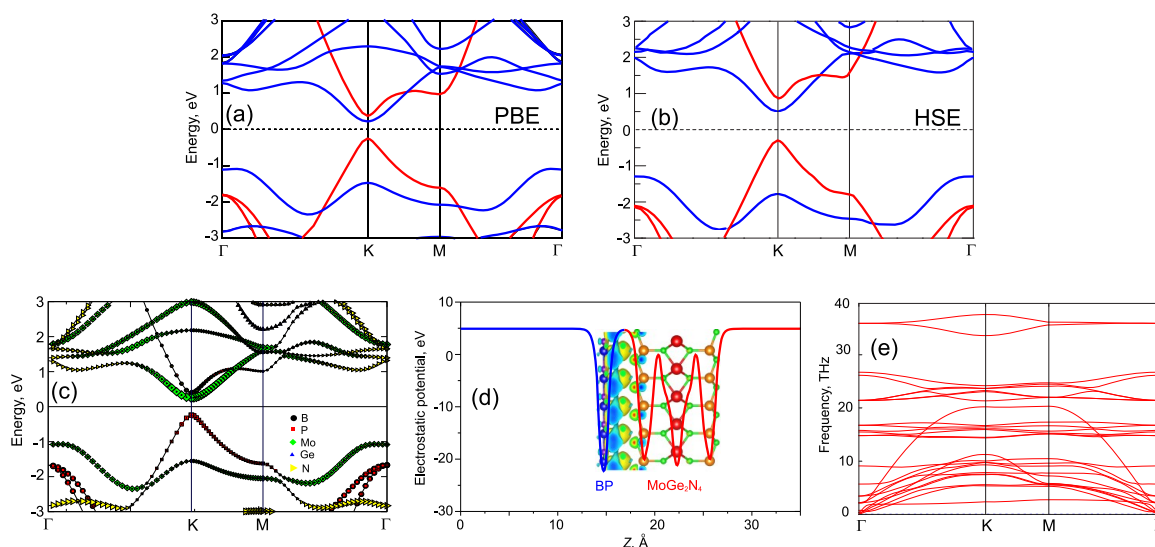
Figure 3. Projected band structures of the BP/MoGe$_2$N$_4$ heterostructure for the most energetically favorable stacking configuration calculated by the (a) PBE and (b) HSE06 method. Red and blue lines represent the contributions of BP and MoGe$_2$N$_4$ layers. (c) Weighted band structure of the most energetically favorable stacking configuration of BP/MoGe$_2$N$_4$. (d) Electrostatic potential and charge density difference in the BP/MoGe$_2$N$_4$ heterostructure. Yellow and cyan regions represent the charge accumulation and depletion, respectively. (e) Phonon dispersion spectrum of BP/MoGe$_2$N$_4$ heterostructure for the most energetically favorable stacking configuration.
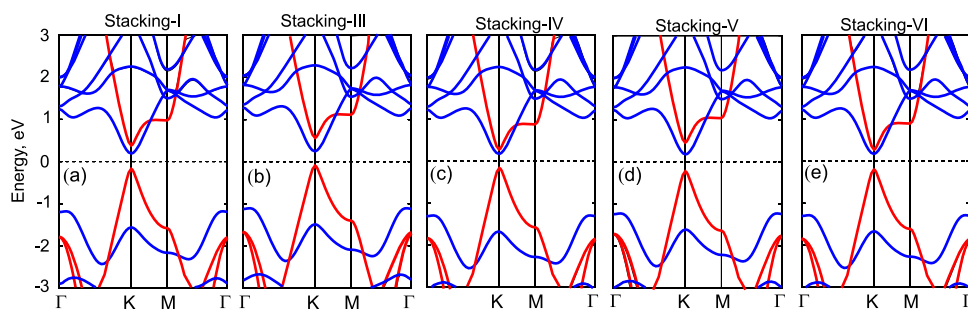

Figure 4. Projected band structures of the BP/MoGe$_2$N$_4$ heterostructure for different stacking configurations, including (a) stacking-I, (b) stacking-III, (c) stacking-IV, (d) stacking-V, and (e) stacking-VI. The dashed line represents the Fermi level, which is set to be zero. The red and blue lines represent the contributions of BP and MoGe$_2$N$_4$ layers, respectively.

structure with stacking-II in the subsequent calculations. The calculated PBE and HSE06 band structures of the most energetically favorable stacking configuration are depicted in Figure 3a and Figure 3b. It is clear that both the PBE and HSE06 shows the same characteristics in the band structure of the BP/MoGe$_2$N$_4$ heterostructure. It exhibits the semiconducting nature with a direct band gap. Both the CBM and VBM of the BP/MoGe$_2$N$_4$ heterostructure are located at the K point. The band gap value of the BP/MoGe$_2$N$_4$ heterostructure is calculated to be 0.47 eV for the PBE and 0.77 eV for the HSE06 method. More interestingly, both PBE and HSE06 methods shows the same trend in the band structure of the BP/MoGe$_2$N$_4$ heterostructure, confirming the reality of the PBE method. Therefore, we used the PBE method for all subsequent calculations due to the high computational cost of the HSE06 method.

The projected band structures of the BP/MoGe$_2$N$_4$ heterostructure for all stacking configurations are depicted in Figure 4. One can find from Figure 3 and Figure 4 that the BP/MoGe$_2$N$_4$ heterostructure exhibits type-II band alignment. The VBM of the BP/MoGe$_2$N$_4$ heterostructure in all stacking configurations comes from the BP layer, whereas the CBM is attributable to the MoGe$_2$N$_4$ layer, confirming the formation of

the type-II band alignment. The electrons and holes are confined in different layers, which can lead to the formation of indirect excitons. Such a formation of type-II band alignment in the BP/MoGe$_2$N$_4$ heterostructure can promote effectively the separation of electrons and holes in real space. This finding thus makes the BP/MoGe$_2$N$_4$ heterostructure a promising candidate for the fabrication of high-performance optoelectronic devices that inhibit carrier recombination. Furthermore, to confirm the formation of the type-II band alignment in the BP/MoGe$_2$N$_4$ heterostructure, we calculate its weighted band structure for the most energetically favorable stacking configurations, as depicted in Figure 3c. It is obvious that the CBM of such heterostructure comes from the Mo-states of MoGe$_2$N$_4$ layer represented by green color, whereas the VBM of heterostructure comes from the P-states of the BP layer, proving the existence of the type-II band alignment.

To visualize the charge redistribution and charge transfer between the BP and MoGe$_2$N$_4$ layers in their corresponding heterostructure, we perform the calculation of charge density difference as follows:

$$\Delta \rho = \rho_{\text{H}} - \rho_{\text{BP}} - \rho_{\text{MGN}} \qquad (2)$$
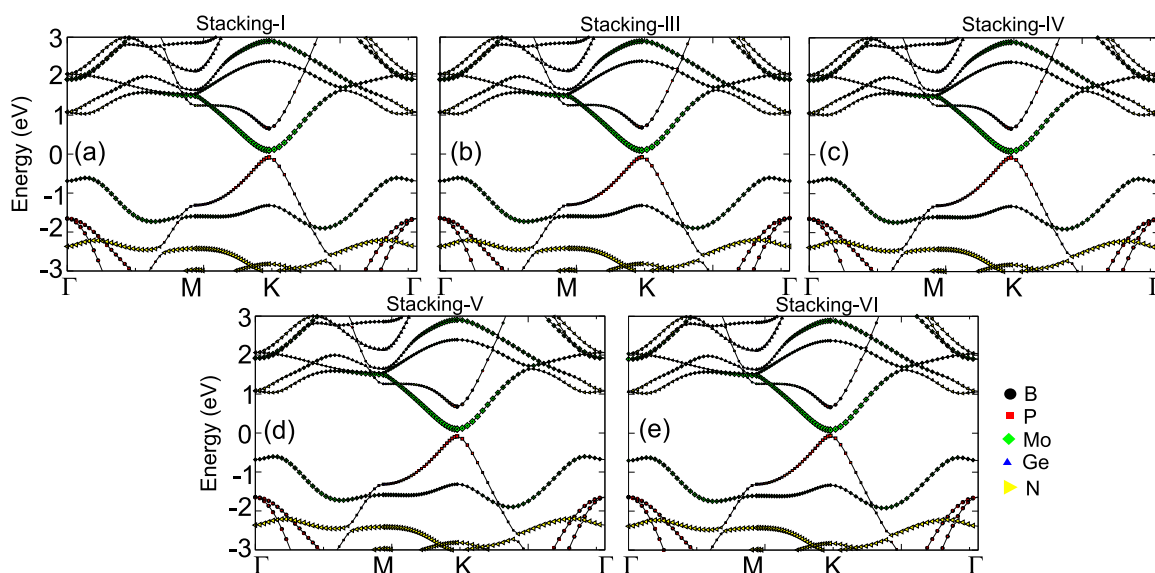
Figure 5. Weighted band structures of the BP/MoGe$_2$N$_4$ heterostructure for different stacking configurations, including (a) stacking-I, (b) stacking-III, (c) stacking-IV, (d) stacking-V, and (e) stacking-VI.

Here, ρ_H, ρ_{BP}, and ρ_{MGN} are the charge densities of the BP/MoGe$_2$N$_4$ heterostructure, isolated BP, and MoGe$_2$N$_4$ monolayers, respectively. The charge density difference of the BP/MoGe$_2$N$_4$ heterostructure is visualized in Figure 3d. In the charge density difference, yellow and cyan regions represent the electron gain and loss, respectively. We observe that the charges are accumulated at the interface region that is close to the MoGe$_2$N$_4$ layer and they are depleted near the BP layer in the BP/MoGe$_2$N$_4$ heterostructure. This feature indicates that the charges are transferred from BP to the MoGe$_2$N$_4$ layers. By Bader charge analysis, we find that there is only a small amount of 0.004 electrons that transferred from BP to the MoGe$_2$N$_4$ layers. In addition, for better understanding of interfacial charge transfer of the BP/MoGe$_2$N$_4$ heterostructure, we calculate the work function and electrostatic potential of the BP/MoGe$_2$N$_4$ heterostructure as well as the constituent monolayers. The work functions of all stacking configurations are listed in Table 1, while the electrostatic potential of the BP/MoGe$_2$N$_4$ heterostructure for the most energetically stacking configuration is depicted in Figure 3d. The work functions of BP and MoGe$_2$N$_4$ monolayers are calculated to be 5.12 and 5.44 eV, respectively. From Table 1, one can find that the work function of the BP/MoGe$_2$N$_4$ heterostructure for different stacking configurations are in the range between that of BP and the MoGe$_2$N$_4$ monolayers. In addition, the difference in the work function of BP and the MoGe$_2$N$_4$ monolayers tends to shift from band alignment and the charge movement in the BP/MoGe$_2$N$_4$ heterostructure.[44−46] The electrostatic potential of the BP/MoGe$_2$N$_4$ heterostructure is depicted in Figure 3d. It can be seen that the BP layer has a lower potential than the MoGe$_2$N$_4$ layer, leading to the formation of potential drop, which will further separate the photogenerated carriers. The phonon spectrum of the BP/MoGe$_2$N$_4$ heterostructure is illustrated in Figure 3e. One can find that there is no negative frequency in the phonon spectrum of the BP/MoGe$_2$N$_4$ heterostructure, confirming that it is dynamically stable.

All calculated band gaps of the BP/MoGe$_2$N$_4$ heterostructure for different stacking configurations are listed in Table 1. We observe that the combination of BP and

MoGe$_2$N$_4$ monolayers to form the BP/MoGe$_2$N$_4$ heterostructure tends to reduce the band gap of the constituent monolayers. The band gap reduction further facilitates the electron excitations. We further plot the weighted band structures, as depicted in Figure 5. One can find that the VBM of such a heterostructure for all stacking configurations is mainly attributable to the P-states of the BP layer, whereas the CBM of the heterostructure comes from the Mo-states of the MoGe$_2$N$_4$ layer. The contributions by different layers to the VBM and CBM of the BP/MoGe$_2$N$_4$ heterostructure confirm the existence of the type-II band alignment in the BP/MoGe$_2$N$_4$ heterostructure.

The optical absorption of materials is calculated as follows:

$$\alpha(\omega) = \frac{\sqrt{2}\,\omega}{c}\{[\varepsilon_1^2(\omega) + \varepsilon_2^2(\omega)]^{1/2} - \varepsilon_1(\omega)\}^{1/2} \tag{3}$$

where $\varepsilon_1^2(\omega)$ and $\varepsilon_2^2(\omega)$ represent the real and imaginary parts of dielectric functions, respectively. The calculated absorption of the BP/MoGe$_2$N$_4$ heterostructure is depicted in Figure 6. The absorption spectra of the constituent BP and MoGe$_2$N$_4$ monolayers are also plotted for comparison. One can find that the BP/MoGe$_2$N$_4$ heterostructure has a wide range of the
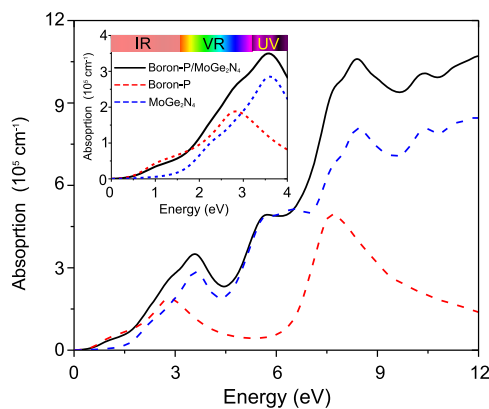

Figure 6. Calculated absorption spectra of BP/MoGe$_2$N$_4$ heterostructure and the constituent BP and MoGe$_2$N$_4$ monolayers.
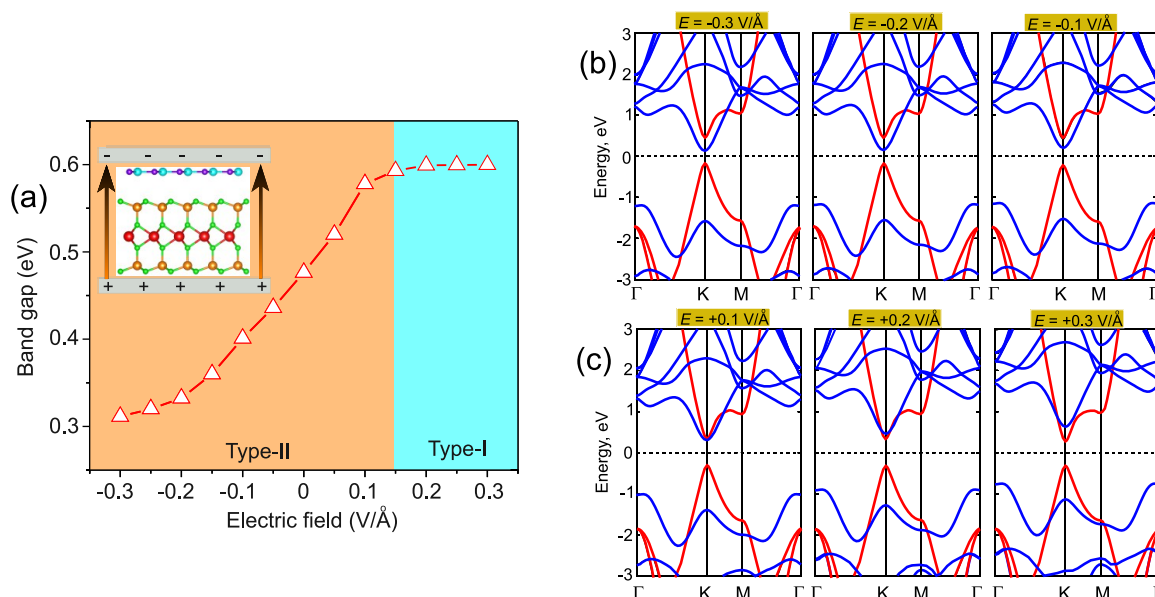
Figure 7. (a) Variation in the band gap of the $BP/MoGe_2N_4$ heterostructure as a function of applied electric field. The inset represents the schematic model of an electric field applied perpendicularly to the heterostructure surface. Projected band structures of $BP/MoGe_2N_4$ heterostructure under the (b) negative and (c) positive electric field. Red and blue lines represent the contributions of BP and $MoGe_2N_4$ layers, respectively.

optical absorption, ranging from the ultraviolet (UV) to the near-infrared (IR). Especially, the $BP/MoGe_2N_4$ heterostructure possesses a large absorption coefficient in the UV light region, which can reach 3.5×10^5 cm^{-1}. In addition, the $BP/MoGe_2N_4$ heterostructure also exhibits an enhancement in the optical absorption in the visible-light around at 3 eV. The absorption coefficient is enhanced up to 3×10^5 cm^{-1}, which is about two times larger than that of BP monolayer.

More interestingly, in the fabrication process of vdW heterostructures, there are some external conditions, such as strain and electric field, which may change the device performance. Therefore, we investigate how these conditions may affect the electronic properties of materials. The electric field is applied perpendicularly to the surface of the $BP/MoGe_2N_4$ heterostructure, as depicted in the inset of Figure 7. The positive direction of the electric field is defined as the direction pointing from the $MoGe_2N_4$ to BP layers with -0.3 V/Å to $+0.3$ V/Å. The change in the band gap of $BP/MoGe_2N_4$ heterostructure with the electric field is depicted in Figure 7a. One can find that applying a negative field tends to decrease the band gap of the $BP/MoGe_2N_4$ heterostructure, whereas the positive field results in an increasing band gap. When the positive electric field is applied to be $+0.15$ V/Å, the band gap of the $BP/MoGe_2N_4$ heterostructure reaches a value of 0.59 eV. Importantly, this electric field strength is close to that achieved in high quality h-BN layers.[38] The band gap is saturated at around 0.59 eV with increasing positive electric field. Such a small change is due to the transition from type-II to type-I band alignment in the $BP/MoGe_2N_4$ heterostructure.

To better understand the mechanisms that underlie the band gap tuning and the band alignment transition of $BP/MoGe_2N_4$ heterostructure, we further plot the projected band structures of the $BP/MoGe_2N_4$ heterostructure under an external electric field in Figure 7b,c. By applying a negative electric field, the band edges of BP and $MoGe_2N_4$ layers move energetically in the opposite directions. The CBM of the BP layer shifts upward far from the Fermi level, whereas the CBM of the

$MoGe_2N_4$ layer moves closer to the Fermi level. Thus, the CBM of the $BP/MoGe_2N_4$ heterostructure in the presence of an external negative electric field is due to the $MoGe_2N_4$ layer. On the other hand, the VBM of the $MoGe_2N_4$ layer shifts downward far from the Fermi level, while the VBM of BP layer moves upward closer the Fermi level. The BP layer thus contributes mainly to the VBM of $BP/MoGe_2N_4$ heterostructure. The shifting of the CBM and VBM under a negative electric field maintains the type-II alignment and decreases the overall band gap of the $BP/MoGe_2N_4$ heterostructures. The mechanism of the tunable electronic properties of the $BP/MoGe_2N_4$ heterostructure under an electric field can be described as such: When a negative electric field is applied, the electrons transfer from the $MoGe_2N_4$ layer to the BP layer. The bands of the $MoGe_2N_4$ layer in this case move downward, while the bands of the BP layer shift upward. On the other hand, when a positive electric field is applied, the electrons transfer from the BP to the $MoGe_2N_4$ layer, and the bands of the BP layer thus move downward, while the bands of the $MoGe_2N_4$ shift upward. On the basis of these mechanisms, the band gap and band alignment of such a heterostructure can be tuned by applying an electric field.

In contrast, the band structures of the $BP/MoGe_2N_4$ heterostructure under a positive electric field exhibits a more dramatic transition (Figure 7c). One can find that the CBM of the BP layer moves closer the Fermi level, whereas its VBM shifts downward far from the Fermi level under a positive electric field. On the other hand, the CBM of the $MoGe_2N_4$ layer moves upward far from the Fermi level and its VBM shifts toward the Fermi level when the positive electric field is applied. When a positive electric field of approximately 0.15 V/ Å is applied, both the CBM and VBM of the $BP/MoGe_2N_4$ heterostructure are dominantly due to the BP layer, resulting in the formation of type-I band alignment. The electric field thus can give rise to the transition from type-II to type-I band alignment in the $BP/MoGe_2N_4$ heterostructure.
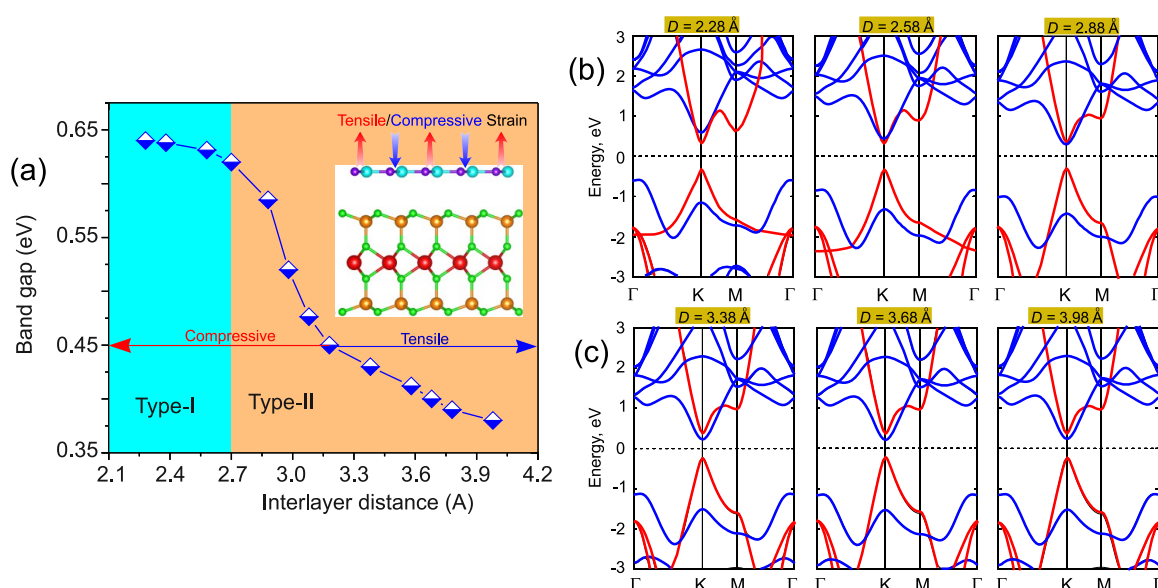
Figure 8. (a) Variation in the band gap of BP/MoGe$_2$N$_4$ heterostructure as a function of interlayer spacing. The inset represents the schematic model of strain engineering. Projected band structures of BP/MoGe$_2$N$_4$ heterostructure under the (b) compressive and (c) tensile strains. Red and blue lines represent the contributions of BP and MoGe$_2$N$_4$ layers, respectively.

We now turn to investigate the effect of strain engineering on the electronic properties of the BP/MoGe$_2$N$_4$ heterostructure by adjusting the interlayer distance. Strain engineering is known to be one of the most effective strategies to control the electronic properties of materials.[47−49] The strain is applied by increasing (tensile) and decreasing (compressive) interlayer distances, as depicted in the inset of Figure 8a. Figure 8a shows the variation of the interlayer distance on the band gap of the BP/MoGe$_2$N$_4$ heterostructure. We find that the band gap of the BP/MoGe$_2$N$_4$ heterostructure is changed nonlinearly as a function of the interlayer distance. The band gap decreases with increasing the tensile strain and it increases with decreasing the compressive strain. The band gap is decreased slowly when the interlayer distance is smaller than 2.58 Å. Such a change is due to the transformation from type-II to type-I band alignment under the compressive strain.

The projected band structures of the BP/MoGe$_2$N$_4$ heterostructure under different interlayer distances are depicted in Figure 8b,c. Under the compressive strain, the CBM of the BP layer moves toward the Fermi level, whereas the CBM of the MoGe$_2$N$_4$ layer shifts upward far from the Fermi level. It shows that when the interlayer distance is shorter than 2.60 Å, the CBM of the BP layer is closer the Fermi level than that of MoGe$_2$N$_4$ layer. The CBM of the BP/MoGe$_2$N$_4$ heterostructure in this case is attributable to the BP layer. Whereas, the VBM of BP moves downward and that of the MoGe$_2$N$_4$ layer shifts toward the Fermi level. The VBM of the BP/MoGe$_2$N$_4$ heterostructure under the compressive strain is attributable to the BP layer. It indicates that the BP/MoGe$_2$N$_4$ heterostructure forms the type-I band alignment when the interlayer distance is shorter than 2.60 Å. Thus, the compressive strain tends to a transformation from type-II to type-I band alignment in the BP/MoGe$_2$N$_4$ heterostructure. The mechanism of such a transformation is attributed to the charge transfer between two layers in their heterostructure. When the compressive strain is applied, the interactions between BP and MoGe$_2$N$_4$ are stronger, and more electrons are transferred from BP to the MoGe$_2$N$_4$ layers. The bands of the BP layer move downward, while those of MoGe$_2$N$_4$ layer

move upward. The band shifts of the BP and MoGe$_2$N$_4$ layers in opposite direction may result in the transition from type-II to type-I band alignment. On the other hand, under the tensile strain, the VBM of the BP/MoGe$_2$N$_4$ heterostructure comes from the BP layer, whereas the CBM is attributable to the MoGe$_2$N$_4$ layer, indicating that the type-II band alignment is maintained. This finding suggests that the tensile strain leads to a decrease in the band gap of BP/MoGe$_2$N$_4$ heterostructure. Our results demonstrate that external electric field and mechanical strain can be used as tuning knobs to control the band alignment and the band gap of the BP/MoGe$_2$N$_4$ heterostructures. Since band alignment and band gap are closely related to optoelectronic device applications, these findings suggest the promising potential of BP/MoGe$_2$N$_4$ in optoelectronic applications.

In summary, we have investigated the structural and electronic properties of the BP/MoGe$_2$N$_4$ heterostructure for different stacking configurations using first-principles calculations. The type-II band alignment, the reduced band gap upon forming heterostructure, and the sizable optical absorption ranging from UV to IR regime suggest a strong potential of BP/MoGe$_2$N$_4$ in optoelectronic applications such as solar energy conversion and photodetection. Interestingly, both the band gap and band alignment of the BP/MoGe$_2$N$_4$ heterostructure can be modulated by an external electric field and vertical strain. The type-II to type-I transition can be achieved when the positive electric field is larger than 0.15 V/Å or when the interlayer spacing is smaller than 2.60 Å. Our findings will open up a new avenue toward vdW heterostructure devices via the synergy of BP and MoGe$_2$N$_4$ monolayers, thus paving a way toward high-performance optoelectronic and photocatalytic nanodevices.

■ AUTHOR INFORMATION

Corresponding Author

Chuong V. Nguyen − *Department of Materials Science and Engineering, Le Quy Don Technical University, Ha Noi*

100000, Vietnam; orcid.org/0000-0002-8365-3343;
Email: chuong.vnguyen@lqdtu.edu.vn

Authors

   Cuong Nguyen − *Department of Physics, University of Education, Hue University, Hue, Vietnam*

   Nguyen V. Hoang − *Department of Materials Science and Engineering, Le Quy Don Technical University, Ha Noi 100000, Vietnam*

   Huynh V. Phuc − *Division of Theoretical Physics, Dong Thap University, Cao Lanh 870000, Vietnam*

   Ang Yee Sin − *Science, Mathematics and Technology (SMT), Singapore University of Technology and Design (SUTD), Singapore 487372, Singapore;* orcid.org/0000-0002-1637-1610

Complete contact information is available at:
https://pubs.acs.org/10.1021/acs.jpclett.1c01284

Notes

The authors declare no competing financial interest.
The data that support the findings of this study are available upon reasonable request from the authors.

■ **REFERENCES**

(1) Novoselov, K. S.; Geim, A. K.; Morozov, S. V.; Jiang, D.; Zhang, Y.; Dubonos, S. V.; Grigorieva, I. V.; Firsov, A. A. Electric Field Effect in Atomically Thin Carbon Films. *Science* **2004**, *306*, 666−669.

(2) Sun, M.; Schwingenschlogl, U. δ-CS: A Direct-Band-Gap Semiconductor Combining Auxeticity, Ferroelasticity, and Potential for High-Efficiency Solar Cells. *Phys. Rev. Appl.* **2020**, *14*, 044015−044020.

(3) Wang, Q. H.; Kalantar-Zadeh, K.; Kis, A.; Coleman, J. N.; Strano, M. S. Electronics and Optoelectronics of Two-Dimensional Transition Metal Dichalcogenides. *Nat. Nanotechnol.* **2012**, *7*, 699−712.

(4) Wang, S.; Ukhtary, M. S.; Saito, R. Strain Effect on Circularly Polarized Electroluminescence in Transition Metal Dichalcogenides. *Phys. Rev. Res.* **2020**, *2*, 033340−033346.

(5) Manzeli, S.; Ovchinnikov, D.; Pasquier, D.; Yazyev, O. V.; Kis, A. 2D Transition Metal Dichalcogenides. *Nat. Rev. Mater.* **2017**, *2*, 17033−17049.

(6) Sun, M.; Yan, Y.; Schwingenschlogl, U. Beryllene: A Promising Anode Material for Na-and K-Ion Batteries with Ultrafast Charge/Discharge and High Specific Capacity. *J. Phys. Chem. Lett.* **2020**, *11*, 9051−9056.

(7) Guan, Z.; Ni, S. Strain-Controllable High Curie Temperature, Large Valley Polarization, and Magnetic Crystal Anisotropy in a 2D Ferromagnetic Janus VSeTe Monolayer. *ACS Appl. Mater. Interfaces* **2020**, *12*, 53067−53075.

(8) Balendhran, S.; Walia, S.; Nili, H.; Sriram, S.; Bhaskaran, M. Elemental Analogues of Graphene: Silicene, Germanene, Stanene, and Phosphorene. *Small* **2015**, *11*, 640−652.

(9) Carvalho, A.; Wang, M.; Zhu, X.; Rodin, A. S.; Su, H.; Neto, A. H. C. Phosphorene: From Theory to Applications. *Nat. Rev. Mater.* **2016**, *1*, 1−16.

(10) Bolotin, K. I.; Sikes, K. J.; Jiang, Z.; Klima, M.; Fudenberg, G.; Hone, J. E.; Kim, P.; Stormer, H. Ultrahigh Electron Mobility in Suspended Graphene. *Solid State Commun.* **2008**, *146*, 351−355.

(11) Xia, F.; Mueller, T.; Lin, Y. M.; Valdes-Garcia, A.; Avouris, P. Ultrafast Graphene Photodetector. *Nat. Nanotechnol.* **2009**, *4*, 839−843.

(12) Xu, X.; Yao, W.; Xiao, D.; Heinz, T. F. Spin and Pseudospins in Layered Transition Metal Dichalcogenides. *Nat. Phys.* **2014**, *10*, 343−350.

(13) Zhu, Z. Y.; Cheng, Y. C.; Schwingenschlögl, U. Giant Spin-Orbit-induced Spin Splitting in Two-Dimensional Transition-Metal Dichalcogenide Semiconductors. *Phys. Rev. B: Condens. Matter Mater. Phys.* **2011**, *84*, 153402−153406.

(14) Nguyen, C. V. Electric Gating and Interlayer Coupling Controllable Electronic Structure and Schottky Contact of Graphene/BiI$_3$ van der Waals Heterostructure. *Phys. Rev. B: Condens. Matter Mater. Phys.* **2021**, *103*, 115429−115436.

(15) Nguyen, H. T.; Obeid, M. M.; Bafekry, A.; Idrees, M.; Vu, T. V.; Phuc, H. V.; Hieu, N. N.; Hoa, L. T.; Amin, B.; Nguyen, C. V. Interfacial Characteristics, Schottky Contact, and Optical Performance of A Graphene/Ga$_2$SSe van der Waals Heterostructure: Strain engineering and electric field tunability. *Phys. Rev. B: Condens. Matter Mater. Phys.* **2020**, *102*, 075414−075423.

(16) Nguyen, T. B.; Cuong, Q. N.; Vu, V. T.; Nguyen, C. V. Interfacial Interfacial Electronic Properties and Tunable Contact Types in Graphene/Janus MoGeSiN$_4$ Heterostructures. *J. Phys. Chem. Lett.* **2021**, *12*, 3934−3940.

(17) Solís-Fernández, P.; Bissett, M.; Ago, H. Synthesis, Structure and Applications of Graphene-Based 2D Heterostructures. *Chem. Soc. Rev.* **2017**, *46*, 4572−4613.

(18) Tan, J.; Avsar, A.; Balakrishnan, J.; Koon, G.; Taychatanapat, T.; O'Farrell, E.; Watanabe, K.; Taniguchi, T.; Eda, G.; Castro Neto, A.; et al. Electronic Transport in Graphene-Based Heterostructures. *Appl. Phys. Lett.* **2014**, *104*, 183504−183507.

(19) Lee, I.; Kang, W. T.; Shin, Y. S.; Kim, Y. R.; Won, U. Y.; Kim, K.; Duong, D. L.; Lee, K.; Heo, J.; Lee, Y. H.; et al. Ultrahigh Gauge Factor in Graphene/MoS$_2$ Heterojunction Field Effect Transistor With Variable Schottky Barrier. *ACS Nano* **2019**, *13*, 8392−8400.

(20) Sun, M.; Chou, J.-P.; Yu, J.; Tang, W. Effects of Structural Imperfection on the Electronic Properties of Graphene/WSe$_2$ heterostructures. *J. Mater. Chem. C* **2017**, *5*, 10383−10390.

(21) Yu, W.; Zhu, Z.; Zhang, S.; Cai, X.; Wang, X.; Niu, C.-Y.; Zhang, W.-B. Tunable Electronic Properties of GeSe/Phosphorene Heterostructure from First-Principles Study. *Appl. Phys. Lett.* **2016**, *109*, 103104−103108.

(22) Huang, Y.; Chen, X.; Wang, C.; Peng, L.; Qian, Q.; Wang, S. Layer-Dependent Electronic Properties of Phosphorene-Like Materials and Phosphorene-Based van der Waals Heterostructures. *Nanoscale* **2017**, *9*, 8616−8622.

(23) Batmunkh, M.; Bat-Erdene, M.; Shapter, J. G. Phosphorene and Phosphorene-Based Materials—Prospects for Future Applications. *Adv. Mater.* **2016**, *28*, 8586−8617.

(24) Li, D.; Xiong, W.; Jiang, L.; Xiao, Z.; Rabiee Golgir, H.; Wang, M.; Huang, X.; Zhou, Y.; Lin, Z.; Song, J.; et al. Multimodal Nonlinear Optical Imaging of MoS$_2$ and MoS$_2$-Based van der Waals Heterostructures. *ACS Nano* **2016**, *10*, 3766−3775.

(25) Li, Z.; Meng, X.; Zhang, Z. Recent Development on MoS$_2$-Based Photocatalysis: A Review. *J. Photochem. Photobiol., C* **2018**, *35*, 39−55.

(26) Sun, Y.; Zhong, W.; Wang, Y.; Xu, X.; Wang, T.; Wu, L.; Du, Y. MoS$_2$-Based Mixed-Dimensional van der Waals Heterostructures: A New Platform for Excellent and Controllable Microwave-Absorption Performance. *ACS Appl. Mater. Interfaces* **2017**, *9*, 34243−34255.

(27) Ningthoujam, R.; Gajbhiye, N. Synthesis, Electron Transport Properties of Transition Metal Nitrides and Applications. *Prog. Mater. Sci.* **2015**, *70*, 50−154.

(28) Mortazavi, B.; Javvaji, B.; Shojaei, F.; Rabczuk, T.; Shapeev, A. V.; Zhuang, X. Exceptional Piezoelectricity, High Thermal Conductivity and Stiffness and Promising Photocatalysis in Two-Dimensional MoSi$_2$N$_4$ Family Confirmed by First-Principles. *Nano Energy* **2021**, *82*, 105716−105728.

(29) Hong, Y. L.; Liu, Z.; Wang, L.; Zhou, T.; Ma, W.; Xu, C.; Feng, S.; Chen, L.; Chen, M. L.; Sun, D. M.; et al. Chemical Vapor Deposition of Layered Two-Dimensional MoSi$_2$N$_4$ Materials. *Science* **2020**, *369*, 670−674.

(30) Cao, L.; Zhou, G.; Wang, Q.; Ang, L.; Ang, Y. S. Two-Dimensional van der Waals Electrical Contact to Monolayer MoSi$_2$N$_4$. *Appl. Phys. Lett.* **2021**, *118*, 013106−013110.

(31) Pham, K. D.; Nguyen, C. Q.; Nguyen, C.; Cuong, P. V.; Hieu, N. V. Two-dimensional van der Waals Graphene/Transition Metal Nitride Heterostructures as Promising High-Performance Nanodevices. *New J. Chem.* **2021**, *45*, 5509−5516.

(32) Şahin, H.; Cahangirov, S.; Topsakal, M.; Bekaroglu, E.; Akturk, E.; Senger, R. T.; Ciraci, S. Monolayer Honeycomb Structures of Group-IV Elements and III-V Binary Compounds: First-Principles Calculations. *Phys. Rev. B: Condens. Matter Mater. Phys.* **2009**, *80*, 155453−155464.

(33) Çakır, D.; Kecik, D.; Sahin, H.; Durgun, E.; Peeters, F. M. Realization of a P−N Junction in a Single Layer Boron-Phosphide. *Phys. Chem. Chem. Phys.* **2015**, *17*, 13013−13020.

(34) Onat, B.; Hallioglu, L.; Ipek, S.; Durgun, E. Tuning Electronic Properties of Monolayer Hexagonal Boron Phosphide With Group III−IV−V Dopants. *J. Phys. Chem. C* **2017**, *121*, 4583−4592.

(35) Mogulkoc, Y.; Modarresi, M.; Mogulkoc, A.; Alkan, B. Electronic and Optical Properties of Boron Phosphide/Blue Phosphorus Heterostructures. *Phys. Chem. Chem. Phys.* **2018**, *20*, 12053−12060.

(36) Obeid, M. M.; Jappor, H. R.; Al-Marzoki, K.; Hoat, D.; Vu, T. V.; Edrees, S. J.; Yaseen, Z. M.; Shukur, M. M. Electronic and Magnetic Properties of Single-Layer Boron Phosphide Associated With Materials Processing Defects. *Comput. Mater. Sci.* **2019**, *170*, 109201−109209.

(37) Zhang, R.; Sun, F.; Zhang, Z.; Liu, J.; Tian, Y.; Zhang, Y.; Wei, X.; Guo, T.; Fan, J.; Ni, L.; et al. Effective Carrier Separation in Zinc Oxide and Boron Phosphide van der Waals Heterostructure. *Appl. Surf. Sci.* **2021**, *535*, 147825−147833.

(38) Hattori, Y.; Taniguchi, T.; Watanabe, K.; Nagashio, K. Layer-By-Layer Dielectric Breakdown of Hexagonal Boron Nitride. *ACS Nano* **2015**, *9*, 916−921.

(39) Giannozzi, P.; Baroni, S.; Bonini, N.; Calandra, M.; Car, R.; Cavazzoni, C.; Ceresoli, D.; Chiarotti, G.; Cococcioni, M.; Dabo, I.; et al. QUANTUM ESPRESSO: A Modular and Open-Source Software Project for Quantum Simulations of Materials. *J. Phys.: Condens. Matter* **2009**, *21*, 395502−395521.

(40) Giannozzi, P.; Andreussi, O.; Brumme, T.; Bunau, O.; Nardelli, M. B.; Calandra, M.; Car, R.; Cavazzoni, C.; Ceresoli, D.; Cococcioni, M.; et al. Advanced Capabilities for Materials Modelling with Quantum Espresso. *J. Phys.: Condens. Matter* **2017**, *29*, 465901−465930.

(41) Perdew, J. P.; Burke, K.; Ernzerhof, M. Generalized Gradient Approximation Made Simple. *Phys. Rev. Lett.* **1996**, *77*, 3865−3868.

(42) Kresse, G.; Joubert, D. From Ultrasoft Pseudopotentials to the Projector Augmented-Wave Method. *Phys. Rev. B: Condens. Matter Mater. Phys.* **1999**, *59*, 1758−1775.

(43) Grimme, S. Semiempirical GGA-Type Density Functional Constructed With a Long-Range Dispersion Correction. *J. Comput. Chem.* **2006**, *27*, 1787−1799.

(44) Liu, B.; Long, M.; Cai, M.-Q.; Yang, J. Two-Dimensional van der Waals Heterostructures Constructed via Perovskite (C$_4$H$_9$NH$_3$)$_2$XBr$_4$ and Black Phosphorus. *J. Phys. Chem. Lett.* **2018**, *9*, 4822−4827.

(45) Liu, B.; Long, M.; Cai, M.-Q.; Yang, J. Interface Engineering of CsPbI$_3$-Black Phosphorus van der Waals Heterostructure. *Appl. Phys. Lett.* **2018**, *112*, 043901−043905.

(46) Liu, B.; Long, M.; Cai, M.; Ding, L.; Yang, J. Interfacial Charge Behavior Modulation in 2D/3D Perovskite Heterostructure for Potential High-Performance Solar Cells. *Nano Energy* **2019**, *59*, 715−720.

(47) He, Y.; Yang, Y.; Zhang, Z.; Gong, Y.; Zhou, W.; Hu, Z.; Ye, G.; Zhang, X.; Bianco, E.; Lei, S.; et al. Strain-Induced Electronic Structure Changes in Stacked van der Waals Heterostructures. *Nano Lett.* **2016**, *16*, 3314−3320.

(48) Chen, D.; Lei, X.; Wang, Y.; Zhong, S.; Liu, G.; Xu, B.; Ouyang, C. Tunable Electronic Structures in BP/MoSSe van der Waals Heterostructures by External Electric Field and Strain. *Appl. Surf. Sci.* **2019**, *497*, 143809−143818.

(49) Li, X.; Jia, G.; Du, J.; Song, X.; Xia, C.; Wei, Z.; Li, J. Type-II InSe/MoSe$_2$ (WSe$_2$) van der Waals Heterostructures: Vertical Strain and Electric Field Effects. *J. Mater. Chem. C* **2018**, *6*, 10010−10019.